DR KUN-HAN LU (Orcid ID : 0000-0002-0355-8515)

PROFESSOR TERRY POWLEY (Orcid ID : 0000-0001-6689-7058)

Article type : Original Article

Automatic Assessment of Human Gastric Motility and Emptying from Dynamic 3D Magnetic Resonance Imaging

Kun-Han Lu[1,3], Zhongming Liu[4,5], Deborah Jaffey[2], John M Wo[6], Kristine Mosier[6], Jiayue Cao[4], Xiaokai Wang[4], Terry L Powley[*2,3]

[1]Weldon School of Biomedical Engineering, Purdue University, West Lafayette, IN, USA

[2]Department of Psychological Sciences, Purdue University, West Lafayette, IN, USA

[3]Purdue Institute for Integrative Neuroscience, Purdue University, West Lafayette, IN, USA

[4]Department of Biomedical Engineering, University of Michigan, Ann Arbor, MI, USA

[5]Department of Electrical Engineering and Computer Science, University of Michigan, Ann Arbor, MI, USA

[6]Indiana University School of Medicine, Indianapolis, IN, USA

Terry L. Powley, PhD

Winer Distinguished Professor of Behavioral Neuroscience

Department of Psychological Sciences

This is the author manuscript accepted for publication and has undergone full peer review but has not been through the copyediting, typesetting, pagination and proofreading process, which may lead to differences between this version and the Version of Record. Please cite this article as doi: 10.1111/NMO.14239

This article is protected by copyright. All rights reserved

College of Health and Human Sciences, Purdue University
703 Third Street
West Lafayette, IN 47907, USA
Phone: +1 765 494 6269
Email: powleyt@purdue.edu

Abstract (250 words)

Background

Time-sequenced magnetic resonance imaging (MRI) of the stomach is an emerging technique for non-invasive assessment of gastric emptying and motility. However, an automated and systematic image processing pipeline for analyzing dynamic 3D (i.e., 4D) gastric MRI data has not been established. This study uses an MRI protocol for imaging the stomach with high spatiotemporal resolution and provides a pipeline for assessing gastric emptying and motility.

Methods

Diet contrast-enhanced MRI images were acquired from seventeen healthy humans after they consumed a naturalistic contrast meal. An automated image processing pipeline was developed to correct for respiratory motion, to segment and compartmentalize the lumen-enhanced stomach, to quantify total gastric and compartmental emptying, and to compute and visualize gastric motility on the luminal surface of the stomach.

Key Results

The gastric segmentation reached an accuracy of 91.10±0.43% with the Type-I error and Type-II error being 0.11±0.01% and 0.22±0.01%, respectively. Gastric volume decreased 34.64±2.8% over 1 hour where the emptying followed a linear-exponential pattern. The gastric motility showed peristaltic patterns with a median = 4 wave-fronts (range 3 - 6) and a mean frequency of 3.09±0.07 cycles per minute. Further, the contractile amplitude was stronger in the antrum than in the corpus (antrum vs. corpus: 5.18±0.24 vs. 3.30±0.16 mm; $p < .001$).

Conclusions & Inferences

Our analysis pipeline can process dynamic 3D MRI images and produce personalized profiles of gastric motility and emptying. It will facilitate the application of MRI for monitoring gastric dynamics in research and clinical settings.

This article is protected by copyright. All rights reserved

Keywords (5-7 keywords)

Gastric emptying, Gastric motility, Image segmentation, Luminal wall motion analysis, Magnetic resonance imaging, Respiratory motion correction

Introduction

Gastric emptying and coordinated motility are crucial to the regulation of food intake and digestion[1]. Dysregulation of gastric emptying and motility can lead to disorders such as dyspepsia[2],

This article is protected by copyright. All rights reserved

gastroparesis[3], and dumping syndrome[4]. Understanding and diagnosis of gastric disorders require direct and comprehensive assessments of gastric function.

Current methods for assessing gastric motility are inadequate, however, because they are either invasive (e.g., antroduodenal manometry[5]), technically cumbersome (e.g., gastric barostat[6]), indirect (e.g., isotope breath test for gastric emptying[7]), or use radioactivity (e.g., gastric scintigraphy[8]). Furthermore, and importantly, none of them is practical for assessing multiple gastric parameters simultaneously, due to the methods' limitations in spatial resolution, temporal resolution, and/or spatial coverage. In contrast, magnetic resonance imaging (MRI) has emerged as a more favorable alternative to assess gastric volume and motility because it is non-invasive and requires no exposure to radiation[9–12]. MRI can produce high spatial resolution images of the entire abdomen with excellent soft-tissue contrast. Recent advancement in MRI scanning technology has also opened the avenue for high-speed acquisition and high temporal resolution monitoring of gastric dynamics[13].

In spite of these advantages, the application of MRI to imaging the stomach has lagged its applications for other organs. Unlike MRI of the brain[14] and the heart[15], no standardized analysis software has been established for the stomach; individual labs or researchers use their home-made routines that are difficult to replicate or adopt broadly. The main technical challenges in developing algorithms for processing gastric MRI data are (1) the complex and convoluted anatomy, (2) respiratory-related movements of the viscera, and (3) variable intraluminal contrast (if an oral contrast agent is applied) of the stomach both within and between individuals. In the past years, several methods have been proposed to segment gastric volume[16–18] and quantify motility[19,20] to address this critical need. However, those methods often require certain user intervention and annotation that could still be laborious and time-consuming. While this may not be an issue for limited-time-point analyses (e.g., gastric emptying test), it can certainly become a challenging task when assessing motility indices from dynamic 3D (or 4D) MRI datasets that consist of numerous images. To promote the adoption of gastric MRI as a standard for diagnosing and monitoring digestive disorders, an automated, streamlined, and objective analysis software is clearly needed.

Here, we present an MRI acquisition protocol and an image processing pipeline for assessing gastric emptying and motility in healthy human volunteers that minimize some of the deficiencies discussed above. Specifically, we developed a naturalistic contrast meal to enhance luminal contrast in T_1-weighted MRI images. With the enhanced contrast and signal-to-noise ratios, we used a rapid image acquisition sequence to assess gastric emptying and motility continuously. Finally, the 4D MRI images were processed with a dedicated pipeline that consisted of respiratory motion correction, stomach

This article is protected by copyright. All rights reserved

segmentation and partition, volumetric analysis of gastric emptying, and surface-based analysis of the frequency, amplitude, and phase relationships of gastric motility. In summary, the experimental protocol and analysis pipeline are expected to help future applications of gastric MRI for quantitative assessment of gastric function in health and disease.

Materials and Methods

Subjects

Seventeen healthy volunteers (10 females; 5 males; plus 2 excluded for excessive residual food in stomach before consuming the test meal) participated in this study under research protocols approved by the Institutional Review Board at Purdue University and Indiana University School of Medicine. Participants who had a prior diagnosis of gastrointestinal (GI), neurological, or psychiatric disorders were excluded. Participants who were taking medications that could affect GI motility were also excluded. Standard MRI exclusion criteria were applied. Informed written consent was obtained from every subject.

Preparation of test meal

The smoothie-like test meal consisted of 350g blended natural ingredients (128g firm tofu, 95g pineapple chunks, 57g pineapple juice, 32g blueberry, and 38g banana). The nutrient content of this meal was as follows: energy (kcal) 236, carbohydrate 74%, protein 13%, fat 7%, and fiber 6%. All ingredients contain a relatively high concentration of manganese, which naturally enhanced signal intensity of the gastric lumen in T_1-weighted MRI images, as shown in Fig. 1.

Experimental design

Every subject was asked to fast for at least 12 hours overnight before MRI. During this period, subjects were asked to avoid any alcohol, caffeine, or medication that could affect gastric function. Subjects were also asked not to drink water for at least 3 hours before the experiment. After setting up the subject in a supine position inside the MRI scanner, a baseline MRI scan was performed before the meal to ensure the subject had fasted properly. Then, the subject sat up on the MRI bed and was asked to consume the test meal at a steady rate within 10 minutes. After meal consumption, post-meal MRI scan sessions (each session lasted for about 5 minutes) were acquired for at least 1 hour. Between scan sessions, each subject was given at least 5 minutes or more of rest when no scanning occurred.

This article is protected by copyright. All rights reserved

MRI acquisition

The MRI scans were performed using a 3T Siemens Prisma MRI scanner with an 18-channel body coil, a 32-channel spine coil, and conventional 3D imaging sequences. The baseline MRI scan was performed using a 3D true fast imaging with steady-state free precession sequence (TRUFI) under free-breathing (repetition time (TR) = 372.7ms; echo time (TE) = 1.85ms; flip angle (FA) = 57^{o}; field-of-view (FOV) = 340×340mm; in-plane resolution = 0.7×0.7mm; 20 coronal slices; slice thickness = 6mm; GRAPPA = 4). Post-meal MRI scans were performed using a 3D Spoiled Gradient Echo Variant sequence (VIBE) under free-breathing (TR = 3.62ms; TE = 1.23ms; FA = 12^{o}; FOV = 360×360mm; in-plane resolution = 1.9×1.9mm; 60 coronal slices; slice thickness = 1.9mm; CAIPIRINHA = 5; partial Fourier factor = 7/8; acquisition time per volume = 3.3-4.2s; 100 volumes were acquired in each scan session). Note that some subjects had their stomach distended more along the posterior-anterior direction. To cover the whole stomach in those subjects, 80 coronal slices were prescribed and thus the acquisition time increased to 4.2s per volume accordingly.

Overview of the image processing pipeline

The steps of the image processing pipeline are schematically illustrated in Fig. 1. The input dataset consisted of multiple sessions of dynamic 3D MRI images that captures both anatomy and physiology. For each session of dynamic 3D MRI images, a respiratory motion correction algorithm was first applied to mitigate movement artifacts induced by breathing. Then, the lumen-enhanced stomach was segmented using an automated atlas-based segmentation algorithm. Specifically, a group-averaged atlas was created from 7 subjects' 3D MRI images, then the associated stomach mask and labels (i.e., fundus, corpus, and antrum) were propagated to the target images through a non-rigid registration process. It is noteworthy that the creation of the group-averaged atlas was a one-time process; it can be applied to new subjects without re-creating or refining the atlas. The segmented and compartmentalized gastric volume was used to compute global and regional gastric emptying, respectively. Then, the surface of the segmented gastric volume was transformed into a wire-frame mesh model for computing motility along the luminal surface. By tracking the motion of every node in the mesh model, this surface-based motility analysis allowed visualization of motility patterns and quantification of the frequency, amplitude, and coordination of peristaltic contractions. Details of each processing step are described in subsequent sections.

Respiratory motion correction

This article is protected by copyright. All rights reserved

Respiration-induced body movements during continuous image acquisition could cause inter-frame misalignments. To mitigate movement artifacts, a non-rigid registration scheme that incorporated a multi-resolution, fast free-form deformation (FFD) approach based on cubic B-splines was applied to align the MRI images[21,22]. The registration algorithm was implemented in MATLAB (Mathworks, Natick, MA). For each session of images, the first 3D image was served as the reference onto which all other images were to be registered. The registration was applied in a multi-resolution fashion to increase the speed and reduce the likelihood of incorrect local registration. Three multiresolution factors, 1/4, 1/2, and 1, were used. Images were first down-sampled by a factor of 1/4 after low-pass filtering to avoid aliasing. The optimal transformation to align two images was obtained by warping a grid of equally spaced (i.e., 16 voxels) control points in x-, y-, and z-directions in the Cartesian coordinate and interpolating in between with cubic B-spline basis functions until the sum-of-squared differences between the two images were minimized. The transform parameters were then used to initialize the registration at the next finer level. This process was repeated until the convergence was achieved at the finest level of image resolution. The parameters associated with the registration algorithm for respiratory motion correction are summarized in Table 1.

Atlas-based segmentation and compartmentalization of the stomach

The lumen-enhanced stomach was segmented by using an automated atlas-based segmentation method. To facilitate image segmentation, a stomach volume atlas containing the lumen-enhanced stomach was first created by applying non-rigid FFD to co-register 3D MRI images of 7 subjects, followed by averaging the aligned images across subjects, as shown in Fig. 2A (the registration parameters are summarized in Table 1). The 7 subjects were the first 7 subjects enrolled in this study, and the 3D MRI images used for creating the atlas were acquired at t = 0 min post-meal (i.e., first image set immediately after meal ingestion). In this stomach volume atlas, the lumen-enhanced stomach was clearly preserved whereas all other unenhanced tissues were smoothed out upon averaging. We observed that including additional subjects' data did not result in a visually different atlas, hence we did not update the atlas as we acquired more subjects' data.

The stomach was manually segmented from the stomach volume atlas and was further partitioned into 3 compartments – fundus, corpus, and antrum (hereinafter refers to as "stomach volume mask and labels"). The stomach partitioning was done by KL and TP, both of whom had over five years of experience reading gastric MRI data. To partition the stomach, we first defined the longitudinal axis of the stomach as the curve that runs from the most proximal point of the stomach wall to the most

This article is protected by copyright. All rights reserved

distal point. Then, we manually defined two anatomical landmarks: one at the angular incisure and the other at the cardiac notch; these two landmarks formed an acute angle on the lesser curvature of the stomach. Lastly, we defined two straight lines that passed through the two landmarks and intersected with the longitudinal axis perpendicularly to partition the stomach into the 3 compartments.

A wire-frame mesh model of the segmented stomach was built in MATLAB to facilitate later surface-based motility assessment. The 3D segmented stomach (i.e., a binary mask) was first smoothed by a box filter (kernel size = 9). Then, a triangulated mesh that contained the mask was created by using MATLAB's *isosurface* function with the iso-value set at 21. The mesh model contained 4,000 vertices (hereinafter refers to as the "stomach surface"); each vertex was labeled with the gastric compartment to which the vertex belonged (Fig. 2A).

The framework of atlas-based segmentation is schematically illustrated in Fig. 2B. The algorithm began by segmenting images in the first session (i.e., t = 0 post-meal). The stomach volume atlas was registered to the first frame of a query subject's MRI images acquired in the first session by using the FFD method (the parameters are summarized in Table 1). Then, the stomach volume mask was propagated to the same MRI image using the result of the registration; this initial segmentation provided a robust estimation of the stomach volume. Subsequently, a 3D deformable model was applied to evolve the boundary of this initial segmentation towards the gastric lumen in each frame, respectively, to achieve a refined segmentation based on local intensity statistic and smoothness criteria[23].

After all frames in the first session were segmented, the first frame in the first session and its segmentation were then used to segment images in the second session by using the same registration-based approach. Briefly, the first frame in the first session was registered to the first frame of the same subject's MRI images acquired in the second session. Then, the segmentation of the first frame in the first session was propagated to the first frame in the second session by using the result of the registration. Finally, all frames in the second session were finely segmented by using the same 3D deformable model approach as aforementioned. This process was repeated until all frames in the last session were segmented.

Following image segmentation, the stomach volume was further partitioned into the fundus, corpus, and antrum in three steps. First, a wire-frame mesh model of the segmented stomach was built in MATLAB similar to how the stomach surface atlas was built; the 3D segmented stomach was first smoothed by a box filter (kernel size = 9), and then the mesh model was created by using MATLAB's isosurface function with the iso-value set at 21. The mesh model contained 4,000 nodes that matched

This article is protected by copyright. All rights reserved

with the number of nodes on the stomach surface atlas. Then, the nodes of the stomach surface atlas were deformed and registered to the nodes of the target stomach through a surface registration process based on the non-rigid iterative closest point algorithm[24]; the surface labels of the three compartments were propagated to the target stomach using the results of the surface registration. Finally, every voxel in the target stomach volume was assigned to one of the compartments according to which surface compartment the voxel was enclosed by, as illustrated in Fig. 2B.

Volumetric analysis of gastric emptying

The volume of the segmented stomach was quantified in its entirety and, regionally, by compartments. Specifically, the segmented voxels within the stomach (or each compartment) were summed over all slices and multiplied by the in-plane resolution and the slice thickness to obtain the imaging-based measurement of the volume. Then, the volumes calculated from the first 3D image in every session were used to quantify both global and regional gastric emptying. Gastric emptying was expressed as percentage change by normalizing the volumes obtained at different times against the volume measured at time 0. Finally, the time series of total gastric and compartmental emptying were resampled at 10-min intervals for every subject and then averaged across subjects.

Surface-based analysis of gastric motility

Here, we describe an automated surface-based analysis of gastric motility by quantifying characteristics of luminal wall motion. Briefly, a non-rigid surface registration algorithm was applied to track the motion of every node in the wire-frame mesh model over time, and gastric motility was characterized as the frequency and amplitude of motion for every node as well as the coordination of motion between nodes. Notably, this surface-based motility assessment allowed direct visualization of the propagation of peristaltic contraction waves along the luminal surface.

The initial steps of the algorithm were the generation of the wire-frame mesh models and tracking of the motion of the nodes in the wire-frame mesh model (Fig. 3A). First, a wire-frame mesh model of 4000 vertices was built from the segmented stomach volume for every frame in a session. Then, an iterative 3D non-rigid surface registration algorithm[24] was used to warp all surface nodes of the first frame outward or inward following locally smooth affine transformations such that the surface was deformed to fit the surface of all subsequent frames; the locally affine deformations were regularized by a stiffness parameter to avoid numerical instabilities. Then, a displacement value was calculated for every node by computing the Euclidean distance of its location in the Cartesian space between the first

This article is protected by copyright. All rights reserved

frame and subsequent frames. After iterating the process through all frames, a displacement time series that represented the luminal wall motion relative to the first time point was obtained for every node in the mesh model (Fig. 3A). With respect to the luminal surface at the first time point, a positive displacement represented deformation in the outward direction (i.e., relaxation), whereas a negative displacement represented deformation in the inward direction (i.e., contraction).

Gastric motility was quantified in terms of the frequency, amplitude, and coordination of gastric contractions (Fig. 3B). The contraction frequency was computed by applying the Fourier transformation to the displacement time series at every node, followed by detecting the dominant frequency in the magnitude of the frequency spectrum. The contraction amplitude was computed by calculating the mean peak-valley difference in the motion time series at every node. Both gastric contraction frequency and amplitude were measured as an entire entity (i.e., the whole stomach) as well as by regions or compartments.

The coordination of gastric contractions was characterized using a seed-based approach that consisted of four steps. First, a master seed was manually localized on the mesh surface of the stomach atlas near the greater curvature of the upper corpus where the pacemaker site was typically located. Secondly, the master seed in the stomach surface atlas was propagated to the target stomach surface through the same iterative 3D non-rigid surface registration algorithm[24]. Then, all motion time series on the target stomach surface were band-pass filtered (0.03–0.07 Hz), and the filtered motion time series within a spherical region of interest (ROI) centered at the master seed location (with a radius of 4 mm) were averaged and used as the seed motion time series. Finally, the phase difference between the seed motion time series and the motion time series of all other nodes was quantified based on Discrete Fourier Transform. The phasic pattern illustrated the coordination of peristaltic contraction waves and also allowed estimation of the number of peristaltic wave-fronts (Fig. 7C).

Statistical analysis

The performance of the respiratory motion correction method was assessed both qualitatively and quantitatively. Qualitative assessment was conducted by generating space-time images that represented the temporal evolution of a pixel-wide line across all frames in a session. Quantitative assessments were carried out by computing two metrics for evaluating the performance: 1) the sum of absolute differences (SAD) metric[25] and 2) the spatial root mean square of the images after temporal differencing (DVARS) metric[26] for all session images. The two metrics were compared before and after applying the respiratory motion correction method.

This article is protected by copyright. All rights reserved

To evaluate the performance of the segmentation method, a total of 30 3D MRI images (2 images were obtained from each subject; the two images were acquired at 0 and 30 minutes after meal consumption, respectively) was manually segmented and used as the ground truth. The investigator who manually processed these images was blinded to the results of the atlas-based segmentation. The accuracy, Type-I error, and Type-II error metrics were obtained for the atlas-based segmentation method based on the ground truth images. Here, the accuracy was defined as Dice Similarity Coefficient[27] (DICE), which represented the degree of spatial overlap between the two segmentation images. The Type-I error was defined as the ratio of the number of background voxels wrongly detected as the foreground (false positive) to the total number of voxels. Similarly, Type-II error was the ratio of the number of foreground voxels wrongly detected as the background (false negative) to the total number of voxels. In addition, Bland-Altman analysis[28] was used to visually assess systemic differences and estimate bias and limits of agreement (LOAs) between the manual segmentation and the atlas-based segmentation. The bias was estimated by the mean volume difference between the two segmentation methods. The LOAs were defined as the 95% confidence interval of volume differences measured by the two segmentation methods.

All statistical analyses were performed using MATLAB. Unless otherwise stated, all data are reported as mean ± standard error of the mean (SEM). The normality of the data was checked using the Kolmogorov-Smirnov test. Student's t-test was performed to compare group means. A probability (P-value) <.05 was considered significant to reject the null hypothesis.

Results

Study population

Two subjects were found to have residual food in their stomach during the initial baseline scan, thus their data were not included in subsequent analyses. Of the remaining 15 subjects, 10 were women. The median age was 31 (range 21-58) years and the mean BMI was 25.2±1.2 kg m^{-2}. The subjects were able to consume the test meal (340±1.9g) within 6.5±0.7 minutes. One baseline MRI scan was acquired from each subject before meal consumption, and a median of 6 (range 4-7) post-meal scan sessions were acquired from these subjects. The difference in the number of post-meal scan sessions across subjects was due to variation in rest intervals between scan sessions (e.g., some subjects needed longer rest intervals).

Respiratory motion correction

This article is protected by copyright. All rights reserved

The overall respiratory motion correction showed an improved alignment between frames within each session. Figure 4A shows example images of space-time representation before and after applying motion correction. Before motion correction, the temporal evolution of an intensity profile sampled across the gastric antrum exhibited abrupt fluctuations around the stomach that were mainly attributed to respiratory movements. Such breathing artifacts were largely, though not entirely, removed after applying motion correction, whereas peristaltic contractions were preserved and became apparent in the space-time representation. A dynamic illustration of the effect of respiratory motion correction is shown in Supplementary Video 1. Figure 4B presents the DVARS and SAD parameters obtained before and after applying motion correction to all subjects' data (113 sessions of data in total). There was a statistically significant effect of motion correction on DVARS and SAD parameters. Specifically, the DVARS parameter was reduced from mean 7.39±0.36 to 5.65±0.24 ($t = 12.44$; $p < .001$), and the SAD parameter was reduced from mean 4.47±0.24 to 3.50±0.16 ($t = 11.30$; $p < .001$). The maximum error of DVARS was reduced from 25.69 to 15.01, and the maximum error of SAD was reduced from 17.00 to 10.22. Both metrics indicated that the degree of misalignment from frame to frame was significantly reduced after motion correction.

Validation of image segmentation

The performance of image segmentation is illustrated in Fig. 5. As can be seen in Figure 5A, the morphology and the contrast of the stomach varies from subject to subject. In spite of this, the atlas-based segmentation method was able to successfully delineate the stomach regardless of its shape and contrast (Figure 5C), comparing to its ground truth segmentation (Figure 5B). Quantitatively, the atlas-based segmentation method reached an accuracy (DICE coefficient) of 91.10±0.43% with the Type-I error being 0.11±0.01% and Type-II error being 0.22±0.01%. The higher Type-II error than Type-I error indicated that the atlas-based segmentation was more likely to have missed segmentation than false segmentation. By visual inspection, the main disagreements between manual and automated methods were mostly attributed to differences at the meal-air interface where luminal intensities and texture were heterogeneous. Figure 5D indicates a regression analysis between the two methods and the corresponding Bland-Altman plot. There was a high correlation between the volumes of gastric meal measured by manual and atlas-based segmentation methods ($r = 0.93$, $p < .001$). Bland-Altman analysis for the total gastric volume measured with the two methods showed a mean bias of a 15.3mL decrease in the atlas-based segmentation (95% LOAs were 14.0mL increase to 44.6mL decrease). The differences

This article is protected by copyright. All rights reserved

in volume measured with the two methods showed a relatively even spread around the estimated mean difference across the range of average volumes.

Volumetric analyses of total gastric and compartmental emptying

The total gastric emptying curve and the compartmental emptying curves of n = 15 subjects are shown in Figure 6. All volumes were normalized against the volume within each respective gastric compartment at time 0, which indicates the percentage of residual volume. During the first 10 minutes, total gastric emptying (Fig. 6A) was mostly attributable to the notably faster volume decrease of the fundus (Fig. 6B). Afterward, the stomach volume decreased mainly due to the emptying of the corpus and antrum (Fig. 6C and 6D). Quantitatively, and specifically for the diet used in this study, the total stomach volume decreased 34.6±2.8% (from 324.7±8.0mL to 212.2±10.5mL) during the first hour; the fundus volume decreased 34.7±8.6% (from 26.6±2.1mL to 17.0±2.3mL) during the first hour; the corpus volume decreased 31.7±4.1% (from 258.5±7.6mL to 167.4±9.0mL) during the first hour, and the antrum volume decreased 26.3±8.6% (from 39.6±2.9mL to 27.8±2.6mL) during the first hour.

Surface-based analysis of gastric motility

The resulting motility patterns and the accompanying animations obtained from the surface-based analysis are shown in Fig. 7 and Supplementary Video 2, respectively. In Supplementary Video 2, peristaltic wave-fronts were initiated near the greater curvature of the upper corpus, oriented orthogonally to the gastric curvatures, and propagated in the longitudinal stomach axis. Notably, the circular muscle peristaltic bands of relaxation (blue) preceding bands of contraction (yellow) towards the antrum and pylorus. The frequency, amplitude, and coordination of peristaltic contractions were then quantified from such dynamic patterns, as shown in Fig. 7. Figure 7A shows the frequency component of gastric motility, where every node on the luminal surface was labeled with the dominant frequency in the motion time series as determined from the power spectral density (PSD) plot. The dominant frequency was found to be uniform across gastric compartments (e.g., 2.6 cycles per minute in this example subject), especially in the corpus and antrum. Similarly, the amplitude component of the gastric motility was calculated and illustrated in Fig. 7B. The amplitude of gastric contractions was found to be stronger along the greater curvature than the lesser curvature. The amplitude of peristaltic contractions also became stronger as they propagated towards the distal antrum. Finally, Fig. 7C shows the coordination map that highlights the phase-difference in motion time series between all surface nodes and the master seed. Such seed-based coordination analysis revealed a phasic organization of peristaltic

This article is protected by copyright. All rights reserved

waves along the longitudinal stomach axis. In this example subject, 3 wave-fronts were observed and the bandwidth was wider towards the greater curvature but narrower towards the lesser curvature. Note that the master seed does not represent the location of the true pace-maker site and can be placed anywhere on the stomach surface that would essentially result in different phasic patterns.

Quantitatively, the dominant frequency of gastric contractions for the whole stomach was 3.09±0.07 cycles per minute (CPM), and no significant differences ($p = .64$) in frequency were found between the corpus (3.09±0.07 CPM) and antrum (3.10±0.07 CPM). Here we only compare the contraction frequency between the corpus and antrum because peristaltic contractions typically only occurred in those two compartments. However, the amplitude of gastric contractions was found to be stronger in the antrum than in the corpus (antrum vs. corpus: 5.18±0.24 vs. 3.30±0.16 mm; $p < .001$). The phasic, coordinated contractile patterns with a median = 4 wave-fronts (range 3 - 6) were observable in all healthy subjects.

Estimation of computation time

All imaging data in this study was processed by using a PC workstation (Intel Xeon CPU E5-2609; 128GB of RAM) with 8 physical cores. Parallel computing was enabled in MATLAB whenever appropriate. It took about 3 hours to process one subjects' data (i.e., 6 sessions), including time required to correct for respiratory motion (90 mins), to segment and partition gastric volumes (60 mins), and to quantify gastric motility (30 mins). To elaborate and compare, our automatic image segmentation algorithm took about 10 minutes to process one session's data (i.e., 100 volumes) [or 1 hour to process one subjects' data (i.e., 6 sessions)]. Compared to automatic segmentation, manual segmentation of the stomach from a 3D volume that consisted of 60 slices took about 15 minutes. The projected manual processing time for a subject (e.g., 100 volumes per session and 6 sessions per study) would require approximately 150 hours to segment all volumes.

Discussion

Previous gastric MRI analyses often relied on a manual or software-assisted boundary tracing process to segment gastric volumes and quantify motility indices. However, this is impractical for processing 4D imaging data which typically contains many images. This has in part limited the wider use of MRI time series for gastric applications.

To promote the application of 4D MRI for gastric analyses, here we present an automated image processing pipeline for capturing and quantifying gastric emptying and motility simultaneously from 4D

This article is protected by copyright. All rights reserved

gastric MRI images. We first introduced an atlas-based segmentation method to automate the delineation and partition of the stomach from 4D MRI data. Notably, we also describe human peristalsis along the stomach wall using a triangulated-mesh representation of the MRI data. By tracking the displacement of nodes on a defined mesh, we were able to automatically quantify the frequency and amplitude of gastric contractions, our surface-based analysis allows direct visualization and quantification of propagation and coordination of peristaltic waves. It is foreseeable that the imaging-based assessment of gastric wall motion can be cross-compared with results obtained from slow-wave activity measured with serosal electrical recordings to investigate spatial and temporal coupling of gastric slow waves[30].

In a recent paper (submitted for publication around the same time as this paper), Sclocco and colleagues introduced a semi-automated processing protocol to quantify gastric emptying and motility indices from 4D cine MRI of the stomach[29]. In their study, the first MRI volume in each session was manually segmented; subsequent volumes were automatically segmented by applying nonlinear geometric deformation to the segmentation result of the first volume. By mapping the same nonlinear deformation field onto the gastric wall surface, they demonstrated the feasibility of capturing gastric wall kinetics with 4D MRI during peristaltic contractions. Although our work and the work by Sclocco and colleagues aim to address very similar scientific purposes, the methodological details are not identical. It awaits future studies to evaluate and compare different methods.

Naturalistic contrast meal for gastric MRI

In this study, we opted to develop a semi-solid meal consisting of blended natural ingredients that are high in manganese content. The working mechanism of manganese ion (Mn^{2+}) is similar to other paramagnetic ions such as gadolinium (Gd^{3+}), which are capable of shortening the T_1 of water protons, thereby increasing the signal intensity of T_1-weighted MRI images[31]. A bright intra-gastric intensity is essential to facilitate automated image segmentation. While the most common contrast meal used in gastric MRI studies is a soup-based diet or caloric liquid nutrient (e.g., Ensure) with the addition of paramagnetic MRI contrast agents (e.g., gadolinium chelates)[32], some studies have proposed to use naturalistic contrast meal such as blueberry or pineapple juice because they contain a high level of manganese[29,33,34]; the use of naturalistic contrast meal is advantageous because it avoids potential safety concerns of an otherwise fabricated contrast agent. Here, we identified that firm tofu is also a high manganese food that contains 1.2mg of manganese per 100g tofu. Mixing firm tofu with other "manganese-rich" fruits into a test meal not only helps match the nutritional content similar to that of

This article is protected by copyright. All rights reserved

the standard western diet for scintigraphy but also increases the viscosity of the meal; the caloric content and viscosity are important factors determining gastric emptying and motility[35,36]. Indeed, as can be seen from Fig. 6, the stomach emptying pattern followed a linear-exponential pattern as described elsewhere for homogenized solids[37] as opposed to a rapid liquid (e.g., fruit juice) emptying pattern which is more exponential-like. Moreover, adding firm tofu also helps neutralize the low PH value of fruit and fruit juice.

Contrast-enhanced gastric MRI under free-breathing

To image both anatomy and physiology, it is desirable for MRI acquisition to cover the stomach in its entirety to capture through-plane motion and monitor its motility continuously. This requires 3D MRI to be collected at high speed without interruption. Abdominal MRI typically requires subjects to hold their breath during image acquisition to avoid respiratory motion artifacts. However, protocols with free-breathing are preferred over breath-hold imaging for physiological reasons. Peristaltic contractions are ultraslow activity (i.e., 3 cycles per minute for stomach in humans[30]), therefore imaging within a single breath-hold (≅20 seconds) is not able to report the full spectrum of evolving gastric dynamics. However, when imaging continuously with a free-breathing protocol, respiration often causes bulk motion, disturbs image quality, and confounds motility assessment. To mitigate this challenge, potential solutions rely on either off-line processing[38] or pulse sequences[29,39] for online correction. In this study, we explored the off-line approach for motion correction.

Analysis and representation of gastric motility on the luminal surface

Conventional GI MRI studies usually quantify GI motility indices either by measuring the depth of contractions[40] or by calculating the diameter (for 2D images) or cross-sectional area (for 3D volumes) change of the lumen at the GI region of interest[19]. However, the former approach could be subjective to where the user chooses to measure the depth of contraction, whereas the latter approach could also be subjective and, in addition, sensitive to the baseline luminal volume. Critically, both methods could be laborious and time-consuming when dealing with 4D imaging data. They are also not ideal for direct visualization and inter-subject alignment, particularly in human subjects.

In this study, we present a workaround by employing an automatic surface-based analysis of the luminal boundary motion in the stomach. The dominant frequency of gastric contraction measured with our automated method (i.e., 3.09±0.07 CPM) showed good correspondence to previously reported frequencies (also around 3CPM) measured with MRI[19,41], scintigraphy[42], manometry[43], or

This article is protected by copyright. All rights reserved

electrogastrogram[30,44]. Uniquely, this surface-based representation provides a way for researchers and clinicians to visualize motility patterns of the entire stomach rather than just within a region of interest, and has the potential to normalize motility patterns across individuals through surface registration.

It is also noteworthy that our MRI data was acquired with isotropic spatial resolution (i.e., 1.9mm) rather than thick-slice image acquisition protocols that are typically used in other gastric MRI studies[29,40]. Isotropic image acquisition not only reduces partial volume effect but can also facilitate more accurate 3D reconstruction of the stomach, which are both critical for surface-based motility analysis. It is foreseeable that a similar analysis may be developed for quantification of lower GI motility, to complete the methodological framework for assessing the physiology and pathological changes in the complete GI system.

Limitations and future directions

There are some limitations in this study. Firstly, our automatic segmentation algorithm was designed to segment high signal intensity voxels (i.e., the contrast meal). This means that any air (which typically appears dark in MRI images) trapped in the stomach was not included in our volume measurement. However, measurement of the entire gastric volume (i.e., meal + air volume) can be essential for evaluating postprandial gastric accommodation in clinical settings, as impaired gastric accommodation is implicated in many gastric disorders[3]. Despite its importance, automatic segmentation of the gastric air is not trivial because the boundary between the air pocket and surrounding tissues is often not well-defined (compared to the boundary of the contrast meal). This is particularly the case when the gastric air pocket is adjacent to the abdominal cavity, which also appears dark in MRI images. Fortunately, there have been strategies warranted to segment the gastric air, though they are mostly semi-automated methods where (minimal) human intervention is required[16,17].

Secondly, the performance of our atlas-based segmentation method was evaluated under a fixed meal (i.e., 350g meal size). We did not try using the same atlas to segment images acquired with different MRI parameters and/or stomachs loaded with a greatly different meal volume. We expect future studies could adopt the same framework by first creating a stomach volume atlas using their own MRI data, and then subsequently use the atlas to segment their MRI images by using a similar registration-based approach. Nevertheless, additional evaluation and validation of our algorithms against stomachs of different size, shapes, and resolution is necessary before its application in clinical settings.

This article is protected by copyright. All rights reserved

Thirdly, we expressed gastric emptying as percentage gastric retention with respect to the volume measured at t = 0 min (i.e., first image set immediately after meal ingestion). Despite we asked subjects to finish the meal within 10 minutes and then prepared the subject into the MRI as quickly as possible, gastric emptying could have already commenced even before the first image set was acquired. Furthermore, acid secretion should be added to the total gastric volume in addition to the meal volume, though we did not measure secretory volume in this study. Therefore, these two potentially confounding factors should be considered when interpreting percentage gastric volume change in this study.

Lastly, the automated image processing pipeline presented in this study relied on several registration processes. The demands on computation power and time are potential limitations for our methods. We envision the processing time of our algorithms can be improved by (1) running the pipeline using a computer cluster, or (2) running the non-rigid registration on a graphical processing unit (GPU) as elaborated elsewhere[45]. Moreover, with the advancement of deep-learning applications for computer vision, we expect that the registration and segmentation process could be accelerated with dedicated deep-learning algorithms.

In summary, our study used a contrast-enhanced MRI method to image and characterize gastric emptying and motility in healthy humans. This method includes free-breathing, fast MRI imaging protocols as well as offline image processing pipelines. Our results demonstrate the potential of using gastric MRI to non-invasively and quantitatively assess multiple gastric parameters.

Acknowledgments

The authors would like to thank Logan A. Chesney for his assistance in creating human expert segmentation of MRI images at Purdue University.

Funding support

This work was supported in part by NIH SPARC 1OT2TR001965 and NIH R01 DK27627.

Data availability statement

The data that support the findings of this study are available from the corresponding author upon reasonable request.

This article is protected by copyright. All rights reserved

References

1. Duthie G, Gardner A. Physiology of the gastrointestinal tract. *John Wiley Sons*. 2006.
2. Tack J, Bisschops R, Sarnelli G. Pathophysiology and treatment of functional dyspepsia. *Gastroenterology*. 2004;127(4):1239-1255.
3. Camilleri M, Chedid V, Ford AC, et al. Gastroparesis. *Nat Rev Dis Prim*. 2018;4(1):1-19.
4. Tack J, Arts J, Caenepeel P, De Wulf D, Bisschops R. Pathophysiology, diagnosis and management of postoperative dumping syndrome. *Nat Rev Gastroenterol Hepatol*. 2009;6(10):583.
5. Hyman PE, Napolitano JA, Diego A, et al. Antroduodenal manometry in the evaluation of chronic functional gastrointestinal symptoms. *Pediatrics*. 1990;86(1):39-44.
6. Azpiroz F, Malagelada J-R. Gastric tone measured by an electronic barostat in health arid postsurgical gastroparesis. *Gastroenterology*. 1987;92(4):934-943.
7. Maes BD, Geypens BJ, Ghoos YF, Hiele MI, Rutgeerts PJ. 13C-octanoic acid breath test for gastric emptying rate of solids. *Gastroenterology*. 1998;114(4):856-857.
8. Abell TL, Camilleri M, Donohoe K, et al. Consensus recommendations for gastric emptying scintigraphy: A joint report of the American Neurogastroenterology and Motility Society and the Society of Nuclear Medicine. *J Nucl Med Technol*. 2008;36(1):44-54.
9. Schwizer W, Steingoetter A, Fox M. Magnetic resonance imaging for the assessment of gastrointestinal function. *Scand J Gastroenterol*. 2006;41(11):1245-1260.
10. De Zwart IM, De Roos A. MRI for the evaluation of gastric physiology. *Eur Radiol*. 2010;20(11):2609-2616.
11. Marciani L. Assessment of gastrointestinal motor functions by MRI: A comprehensive review. *Neurogastroenterol Motil*. 2011;23(5):399-407.
12. de Jonge CS, Smout AJPM, Nederveen AJ, Stoker J. Evaluation of gastrointestinal motility with MRI: Advances, challenges and opportunities. Neurogastroenterol Motil. 2018;30(1), e13257.
13. Hamilton J, Franson D, Seiberlich N. Recent advances in parallel imaging for MRI. *Prog Nucl Magn Reson Spectrosc*. 2017;101:71-95.
14. Smith SM, Jenkinson M, Woolrich MW, et al. Advances in functional and structural MR image

This article is protected by copyright. All rights reserved

analysis and implementation as FSL. *Neuroimage*. 2004;23:S208-S219.

15. Almutairi HM, Khanji MY, Boubertakh R, Miquel ME, Petersen SE. A comparison of cardiac motion analysis software packages: application to left ventricular deformation analysis in healthy subjects. *J Cardiovasc Magn Reson*. 2016;18(422).
16. Bharucha AE, Karwoski RA, Fidler J, et al. Comparison of manual and semiautomated techniques for analyzing gastric volumes with MRI in humans. *AJP Gastrointest Liver Physiol*. 2014;307(5):G582-G587.
17. Banerjee S, Dixit S, Fox M, Pal A. Validation of a rapid, semiautomatic image analysis tool for measurement of gastric accommodation and emptying by magnetic resonance imaging. *Am J Physiol - Gastrointest Liver Physiol*. 2015;308(8):G652-G663.
18. Banerjee S, Pal A, Fox M. Volume and position change of the stomach during gastric accommodation and emptying: A detailed three-dimensional morphological analysis based on MRI. *Neurogastroenterology & Motility.* 2020;32(8):e13865.
19. Bickelhaupt S, Froehlich JM, Cattin R, et al. Software-supported evaluation of gastric motility in MRI: A feasibility study. *J Med Imaging Radiat Oncol*. 2014;58(1):11-17.
20. Menys A, Hoad C, Spiller R, et al. Spatio-temporal motility MRI analysis of the stomach and colon. *Neurogastroenterol Motil*. 2019;31(5):1-9.
21. Rueckert D, Sonoda LI, Hayes C, Hill DLG, Leach MO, Hawkes DJ. Nonrigid registration using free-form deformations: application to breast MR images. *IEEE Trans Med Imaging*. 1999;18(8):712-721.
22. Myronenko A, Song X. Intensity-based image registration by minimizing residual complexity. *IEEE Trans Med Imaging*. 2010;29(11):1882-1891.
23. Lankton S, Tannenbaum A. Localizing region-based active contours. *IEEE Trans image Process*. 2008;17(11):2029-2039.
24. Amberg B. Optimal Step Nonrigid ICP Algorithms for Surface Registration. *CVPR*. 2007.
25. Hill DLG, Batchelor PG, Holden M, Hawkes DJ. Medical image registration. *Phys Med Biol*. 2001;46(3):R1.
26. Power JD, Barnes KA, Snyder AZ, Schlaggar BL, Petersen SE. Spurious but systematic correlations in functional connectivity MRI networks arise from subject motion. *Neuroimage*. 2012;59(3):2142-2154.
27. Fleiss JL, Levin B, Paik MC. The measurement of interrater agreement. *Stat methods rates proportions*. 1981;2(212-236):22-23.

This article is protected by copyright. All rights reserved

28. Bland JM, Altman D. Statistical methods for assessing agreement between two methods of clinical measurement. *Lancet*. 1986;327(8476):307-310.
29. Sclocco R, Nguyen C, Staley R, et al. Non-uniform gastric wall kinematics revealed by 4D Cine magnetic resonance imaging in humans. *Neurogastroenterol Motil*. 2021; e14146.
30. O'Grady G, Du P, Cheng LK, et al. Origin and propagation of human gastric slow-wave activity defined by high-resolution mapping. *Am J Physiol - Gastrointest Liver Physiol*. 2010;299(3):G585-G592.
31. Pan D, Schmieder AH, Wickline SA, Lanza GM. Manganese-based MRI contrast agents: past, present and future. *Tetrahedron*. 2011;67(44):8431.
32. Hoad CL, Parker H, Hudders N, et al. Measurement of gastric meal and secretion volumes using magnetic resonance imaging. *Phys Med Biol*. 2015;60(3):1367-1383.
33. Zarrini M, Seilanian Toosi F, Davachi B, Nekooei S. Natural Oral Contrast Agents for Gastrointestinal Magnetic Resonance Imaging. 2015;2(4), 200-204.
34. Elsayed NM, Alsalem SA, Almugbel SAA, Alsuhaimi MM. Effectiveness of natural oral contrast agents in magnetic resonance imaging of the bowel. Egypt J Radiol Nucl Med. 2015;46(2), 287-292.
35. Kwiatek MA, Menne D, Steingoetter A, et al. Effect of meal volume and calorie load on postprandial gastric function and emptying: studies under physiological conditions by combined fiber-optic pressure measurement and MRI. *AJP Gastrointest Liver Physiol*. 2009;297(5):G894-G901.
36. Marciani L, Gowland P a, Spiller RC, et al. Effect of meal viscosity and nutrients on satiety, intragastric dilution, and emptying assessed by MRI. *Am J Physiol Gastrointest Liver Physiol*. 2001;280(6):G1227-G1233.
37. Zinsmeister AR, Bharucha AE, Camilleri M. Comparison of calculations to estimate gastric emptying half-time of solids in humans. *Neurogastroenterol Motil*. 2012;24(12):1142-1145.
38. Menys A, Hamy V, Makanyanga J, et al. Dual registration of abdominal motion for motility assessment in free-breathing data sets acquired using dynamic MRI. *Phys Med Biol*. 2014;59(16):4603-4619.
39. Deng Z, Pang J, Yang W, et al. Four-dimensional MRI using three-dimensional radial sampling with respiratory self-gating to characterize temporal phase-resolved respiratory motion in the abdomen. *Magn Reson Med*. 2016;75(4):1574-1585.
40. Cho J, Jin Y, Id L, et al. Quantitative MRI evaluation of gastric motility in patients with Parkinson's

This article is protected by copyright. All rights reserved

disease : Correlation of dyspeptic symptoms with volumetry and motility indices. *PLoS One*. 2019;14(5):1-14.

41. de Jonge CS, Sprengers AMJ, van Rijn KL, Nederveen AJ, Stoker J. Assessment of fasted and fed gastrointestinal contraction frequencies in healthy subjects using continuously tagged MRI. *Neurogastroenterol Motil*. 2020;32(2):1-8.
42. Orthey P, Dadparvar S, Kamat B, Parkman HP, Maurer AH. Using gastric emptying scintigraphy to evaluate antral contractions and duodenal bolus propagation. *Am J Physiol - Gastrointest Liver Physiol*. 2020;318(1):G203-G209.
43. Patcharatrakul T, Gonlachanvit S. Technique of functional and motility test: How to perform antroduodenal manometry. *J Neurogastroenterol Motil*. 2013;19(3):395-404.
44. Wolpert N, Rebollo I, Tallon-Baudry C. Electrogastrography for psychophysiological research: Practical considerations, analysis pipeline, and normative data in a large sample. *Psychophysiology*. 2020; 57(9):e13599.
45. Modat M, McClelland J, Ourselin S. Lung registration using the NiftyReg package. *Med image Anal Clin Gd Chall*. 2010; 33-42.

Tables

FFD parameters	Respiratory motion correction	Stomach atlas creation	Atlas-based segmentation
Similarity measure	Sum of squared differences	Correlation coefficient	Correlation coefficient
Multiresolution factor	3 levels	3 levels	3 levels
Control-point spacing	16 voxels	8 voxels	8 voxels

Table 1. Fast free-form deformation parameters for image registration processes applied in respiratory motion correction, stomach atlas creation, and atlas-based segmentation.

Figure legends

Figure 1. A workflow for acquisition and automated analysis of dynamic 3D gastric MRI data in humans. Dynamic 3D diet contrast-enhanced gastric MRI was acquired with multiple-receiver abdominal coil and parallel imaging sequences. Then, an automated non-rigid registration algorithm was applied to correct for respiratory motion. After motion correction, the lumen-enhanced stomach was delineated using an atlas-based approach; the atlas was created from 7 subjects' 3D MRI images, and the atlas

This article is protected by copyright. All rights reserved

creation step was a once-and-for-all process. Gastric and compartmental emptying was computed from the segmented and partitioned stomach volume. Next, a wire-frame mesh model was created from the surface of the segmented stomach. Luminal wall motion (i.e., contraction or relaxation) was estimated for every node in the wire-frame mesh model through a non-rigid surface registration algorithm. Finally, the frequency, amplitude, and coordination of peristaltic contractions were quantified from the luminal wall motion using the surface-based motility analysis.

Figure 2. Atlas creation and atlas-based segmentation of the stomach. (A) A stomach volume atlas was created by non-rigidly registering 6 subject's 3D MRI image to 1 reference image. The lumen-enhanced stomach was manually segmented from the stomach volume atlas, followed by partitioning the stomach into 3 compartments: fundus, corpus, and antrum. Then, a stomach surface model and its compartmental labels were created from the segmented stomach volume. **(B)** An atlas-based approach was applied to segment and partition the target MRI image. The stomach volume atlas was non-rigidly registered to the target image, followed by propagating the stomach volume mask to the target image space using the results of the registration. The propagated segmentation served as an initial estimate of the stomach volume, which was subsequently refined by using a 3D deformable model. Finally, the segmented target stomach was partitioned based on the transformed atlas labels.

Figure 3. Surface-based analysis of gastric motility. (A) After building a wire-frame mesh model from the segmented stomach volume for every frame in a session, the luminal wall motion is estimated for every node in the mesh model using a non-rigid surface registration algorithm. Specifically, the algorithm tracks the displacement of nodes (with respect to their position at t = 0) while deforming the stomach surface of the first frame outward or inward until it is aligned with the surface of all subsequent frames. A positive displacement represents relaxation (green) whereas a negative displacement indicates contraction (red). After iterating the process through all frames, a time series that represented the luminal wall motion can be obtained for every node in the mesh model. **(B)** The frequency and amplitude can be directed estimated from the motion time series for every node, whereas the coordination of peristaltic contractions was quantified by calculating the phasic index between pairs of motion time series.

Figure 4. Performance evaluation of respiratory motion correction algorithm. (A) Space-time representation of an intensity profile sampled across the gastric antrum. The location of the sampling

This article is protected by copyright. All rights reserved

line is indicated by a red dashed line in the MRI image. The temporal evolution of the intensity profile shows abrupt fluctuations around the stomach that were mainly attributed to breathing movements. Such breathing artifacts were largely removed after applying motion correction where peristaltic contractions become apparent. **(B)** Box and whisker plot of registration error before and after motion correction. DVARS: the spatial root mean square of images after temporal differencing. SAD: Sum of absolute differences.

Figure 5. Representative examples of atlas-based segmentation of gastric meal volume. (A) Original images. **(B)** Ground truth segmentation performed by a human expert. **(C)** Atlas-based segmentation. The atlas-based approach yields high agreement with the ground truth except at the meal-air interface. **(D)** Top panel: Scatter plot of gastric volumes measured by the manual versus atlas-based segmentation. The solid line shows the line of regression fitted using a least-squares method (with coefficient of 0.97; R^2 =0.87; p<.001). The interrupted line shows the line of identity. Bottom panel: Bland-Altman plot for the gastric volumes measured by the manual segmentation versus atlas-based segmentation. Closed circles: the 7 images collected at t = 0 for creating the stomach volume atlas. Open circles: other images that were not used to create the stomach volume atlas.

Figure 6. Total and compartmental gastric emptying profiles. (A) Stomach emptying profile. **(B)** Fundus emptying profile. **(C)** Corpus emptying profile. **(D)** Antrum emptying profile. All volumes were normalized against the volume at time 0. Values are mean ± standard error of the mean.

Figure 7. Surface representation of gastric motility. (A) Frequency component of gastric motility. The dominant frequency was determined from the power spectral density (PSD) of motion time series for every node (the circles) on the luminal surface. **(B)** Amplitude component of gastric motility. The amplitude was calculated from the mean peak-valley difference in the motion time series. **(C)** Coordination of peristaltic contractions. A phasic index (i.e., the phase difference between the two time series) was determined between the motion time series of a node and the time series averaged around the master seed (with a radius of 4mm). In this example subject, 3 peristaltic wavefronts can be observed.

This article is protected by copyright. All rights reserved

Supplementary Video 1. Dynamic illustration of the effect of respiratory motion correction. The images are maximum intensity projection of the original 3D images. The display frame rate was set at 5 frames per second. The actual time interval between frames is 3.3 seconds.

Supplementary Video 2. Dynamic illustration of a surface representation of human peristalsis. Peristaltic wave-fronts were initiated near the greater curvature of the upper corpus, oriented orthogonally to the gastric curvatures, and propagated in the longitudinal stomach axis. The circular muscle peristaltic bands of relaxation (blue) preceding bands of contraction (yellow) towards the antrum and pylorus. The display frame rate was set at 5 frames per second. The actual time interval between frames is 3.3 seconds.

This article is protected by copyright. All rights reserved

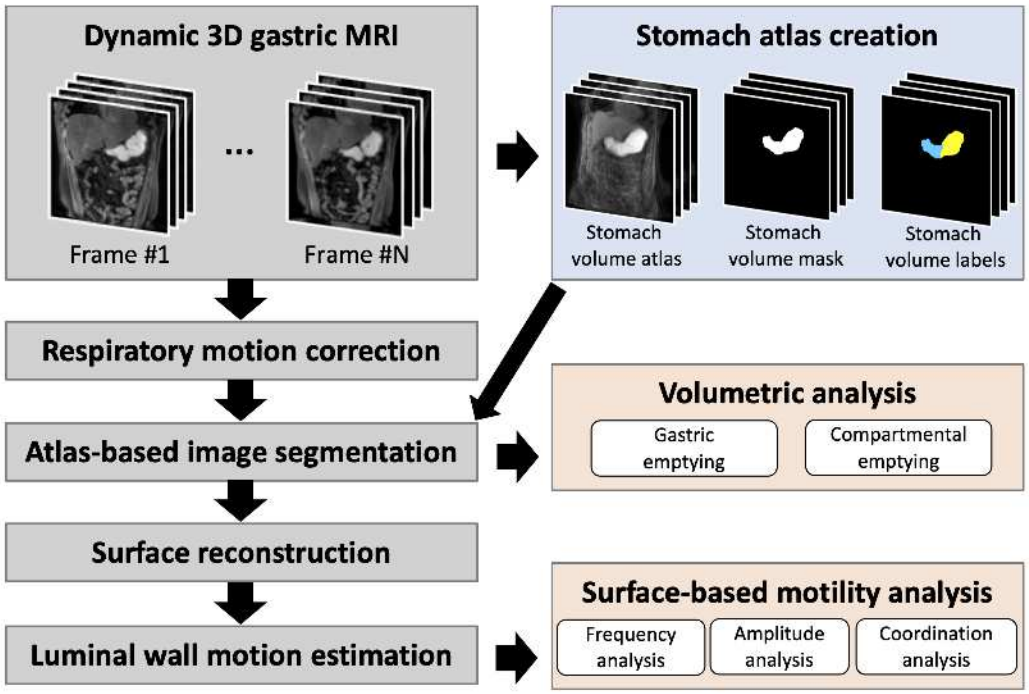

nmo_14239_f1.tiff

This article is protected by copyright. All rights reserved

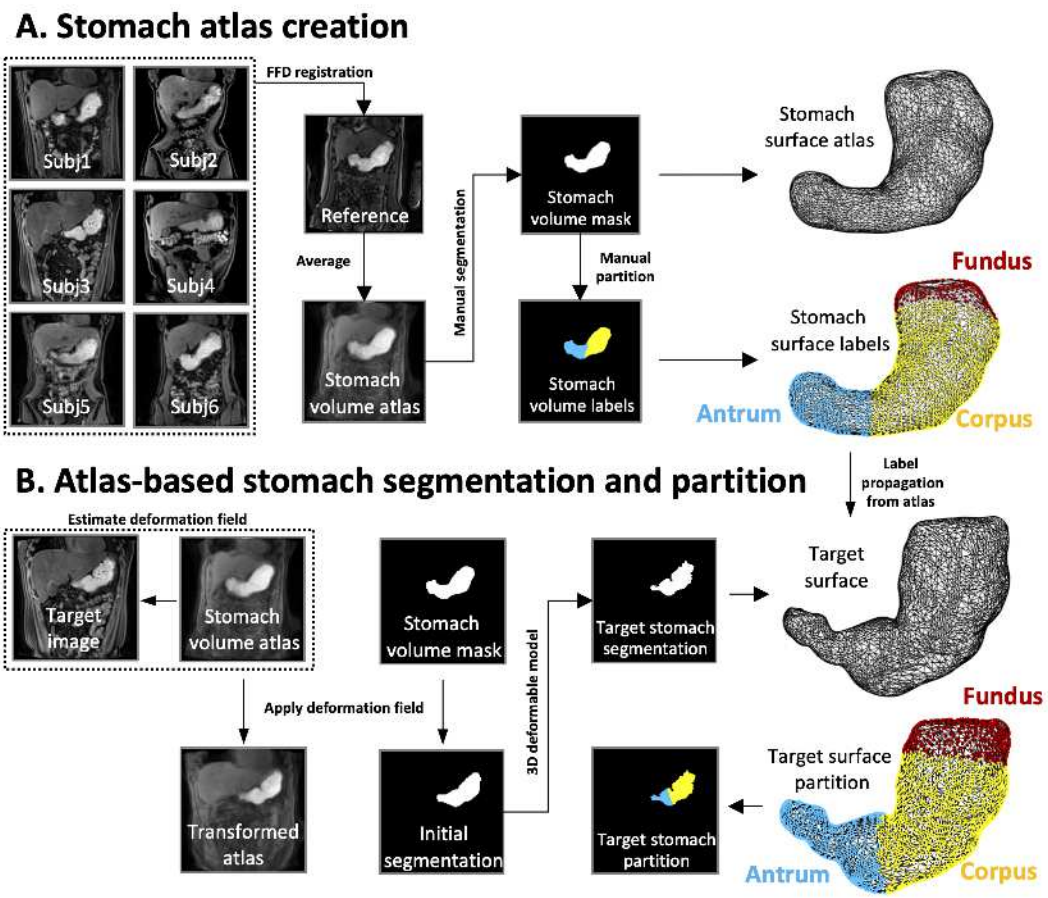

nmo_14239_f2.tiff

This article is protected by copyright. All rights reserved

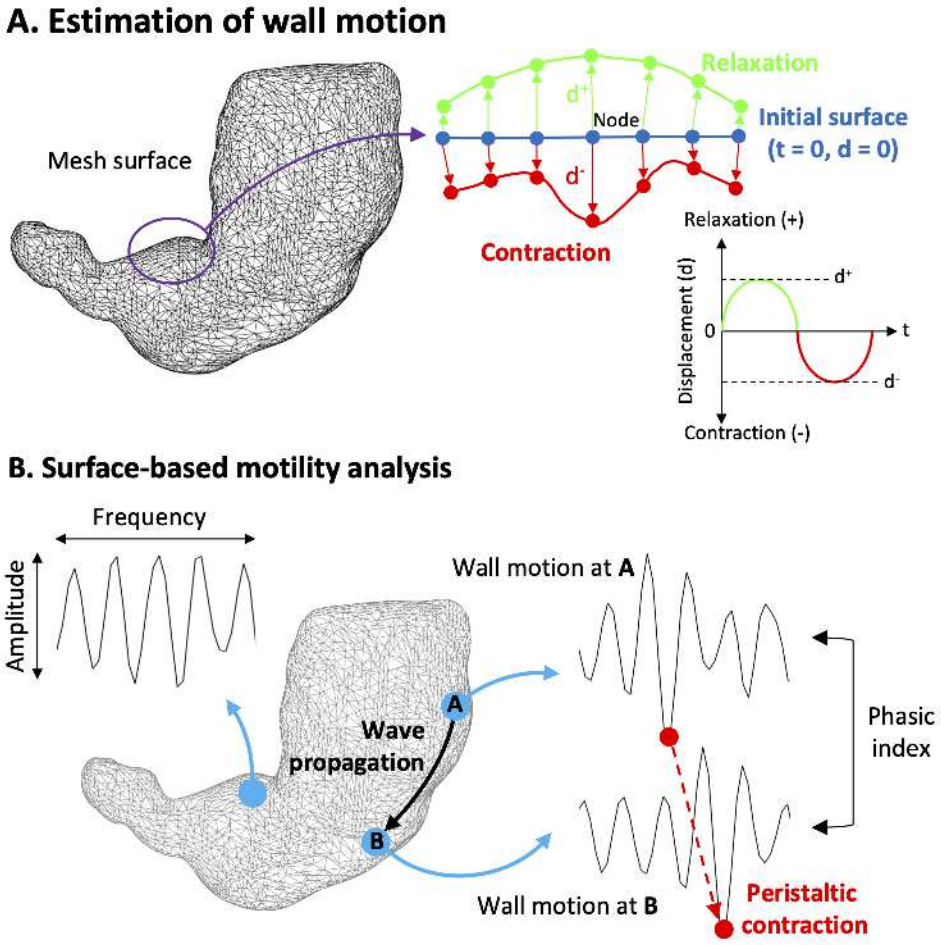

nmo_14239_f3.tiff

This article is protected by copyright. All rights reserved

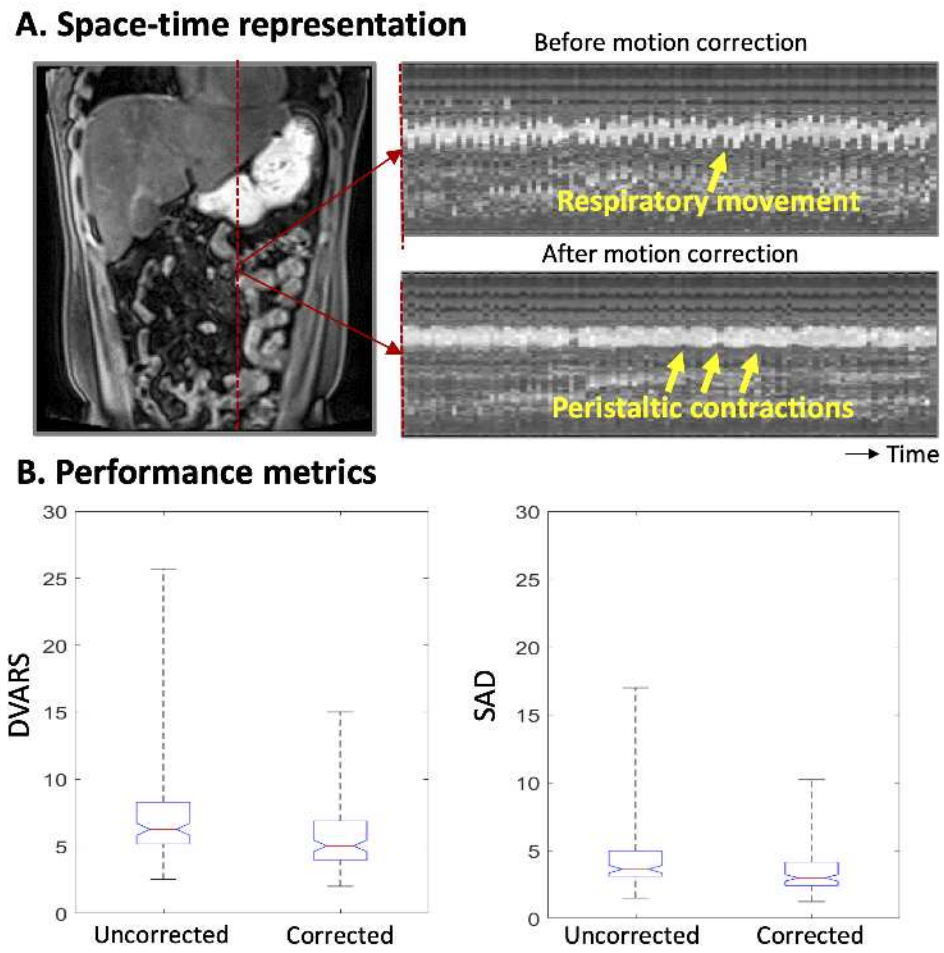

nmo_14239_f4.tiff

This article is protected by copyright. All rights reserved

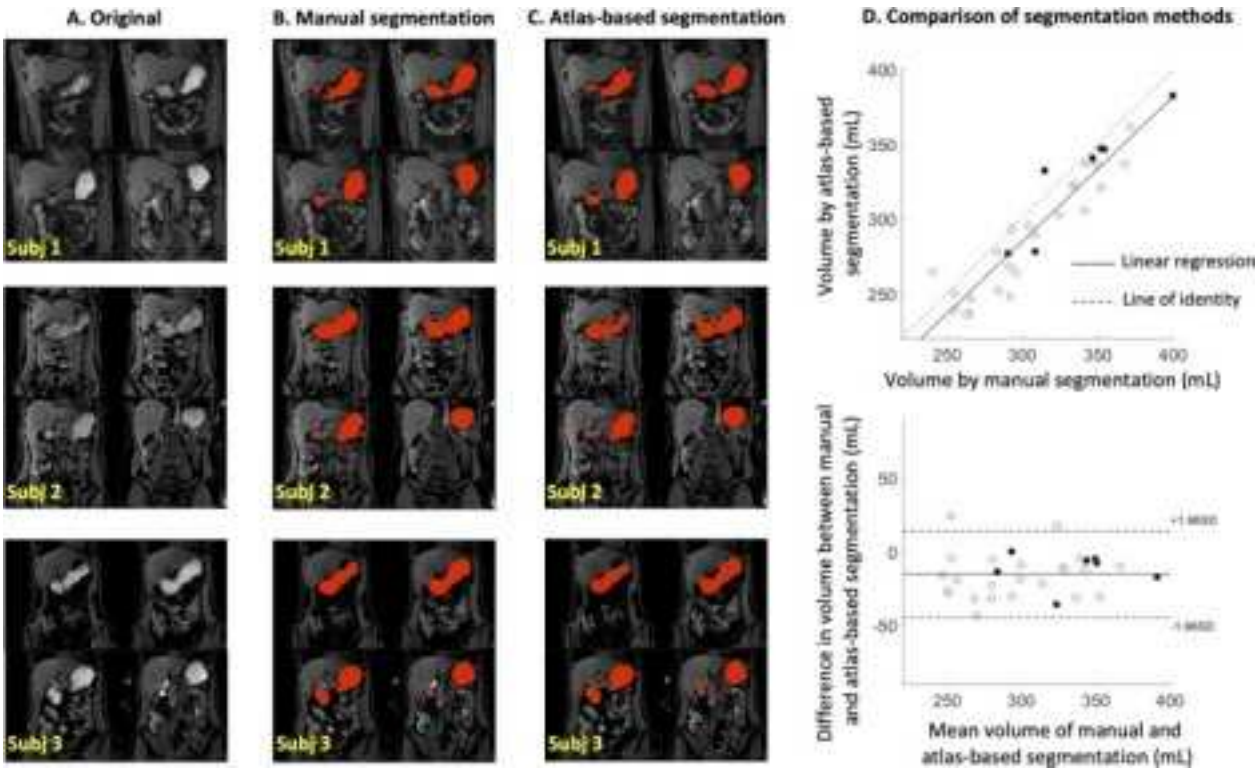

nmo_14239_f5.tiff

This article is protected by copyright. All rights reserved

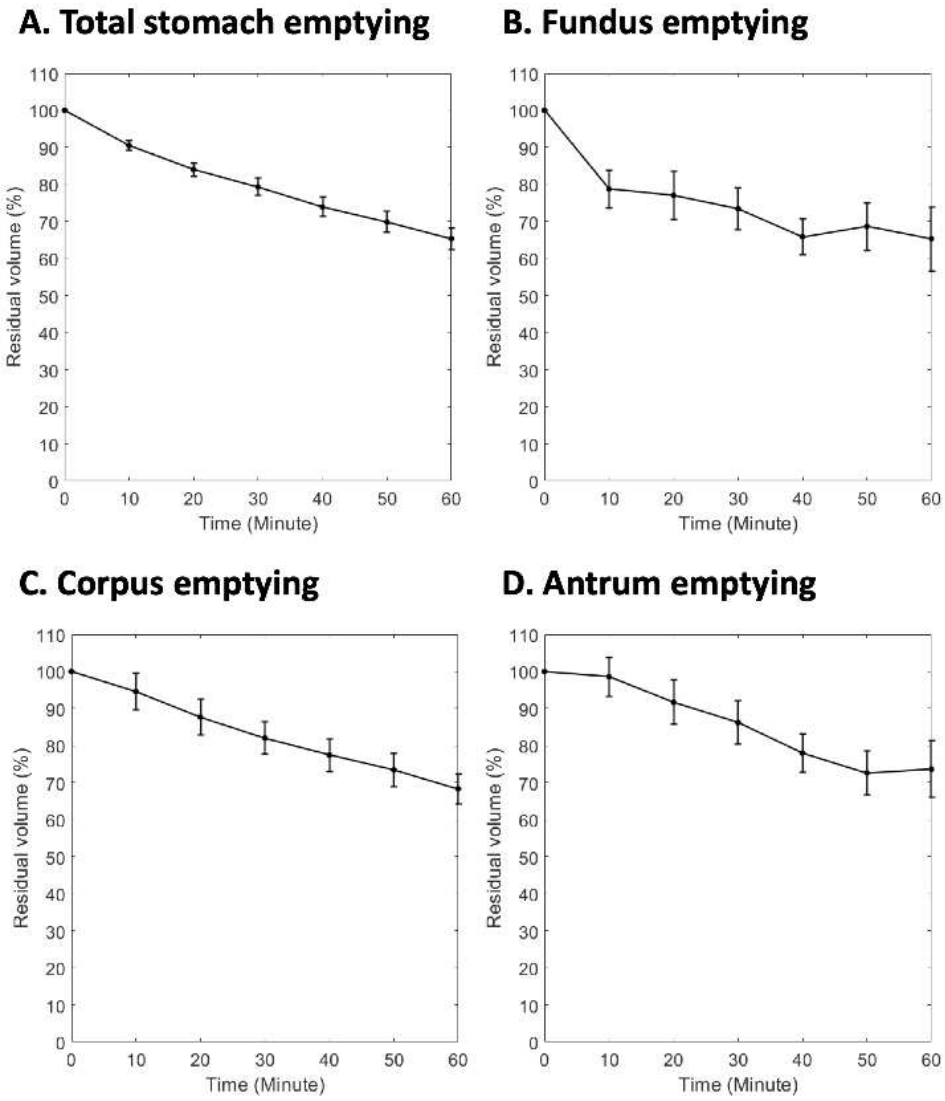

nmo_14239_f6.tiff

This article is protected by copyright. All rights reserved

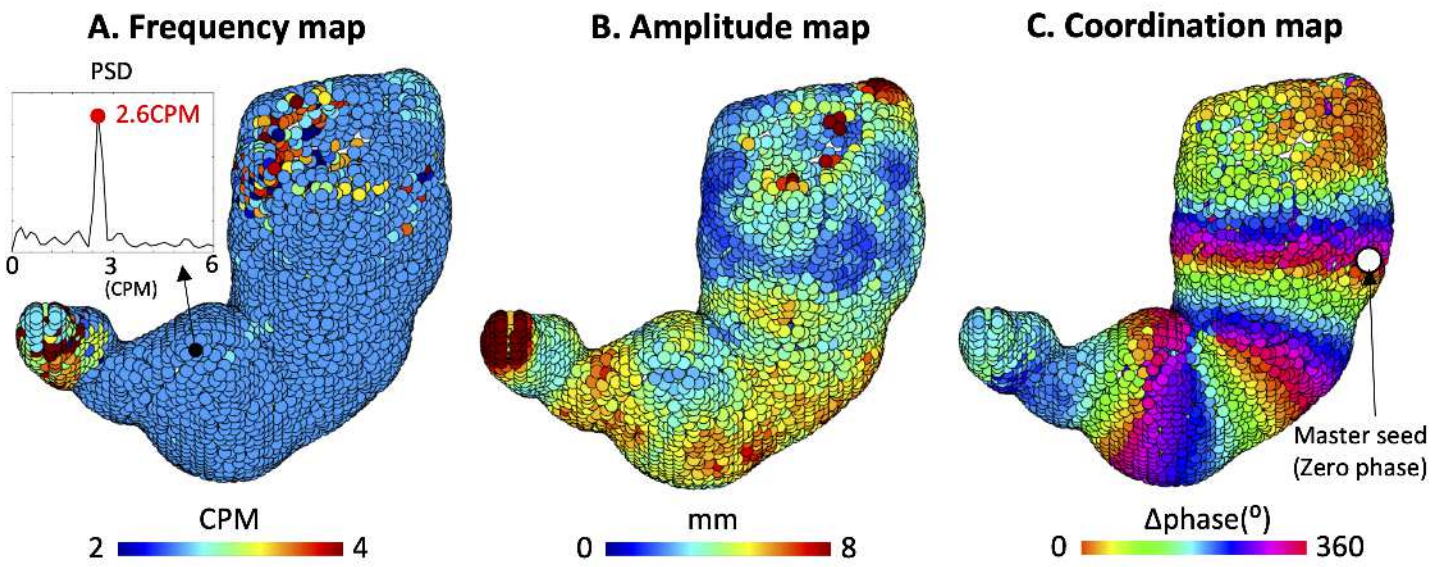

nmo_14239_f7.tiff

This article is protected by copyright. All rights reserved